PHYSICAL REVIEW C **89**, 024616 (2014)

Production cross sections of heavy neutron-rich nuclei approaching the nucleosynthesis *r*-process path around $A = 195$

T. Kurtukian-Nieto,[1,*] J. Benlliure,[1] K.-H. Schmidt,[2] L. Audouin,[3] F. Becker,[2,†] B. Blank,[4] E. Casarejos,[1,‡] F. Farget,[5] M. Fernández-Ordóñez,[1] J. Giovinazzo,[4] D. Henzlova,[2,§] B. Jurado,[4] J. Pereira,[1,‖] and O. Yordanov[2,¶]

[1]*Departmento de Física de Partículas, Universidade de Santiago de Compostela, E-15782 Santiago de Compostela, Spain*

[2]*GSI-Helmholtzzentrum für Schwerionenforschung GmbH, D-64291 Darmstadt, Germany*

[3]*Institut de Physique Nucléaire, F-91406 Orsay, France*

[4]*Centre d'Etudes Nucléaires de Bordeaux Gradignan (CENBG), UMR 5797 IN2P3/CNRS-Université Bordeaux, F-33170 Gradignan, France*

[5]*GANIL, BP55025, F-14076 Caen Cedex 5, France*

(Received 17 December 2013; published 27 February 2014)

In the present work we were able to synthesize and measure with high accuracy the production cross sections of more than 190 heavy neutron-rich nuclei by the in-flight fragmentation of relativistic ^{208}Pb projectiles, 26 of which were produced for the first time. This work has shown that the $N = 126$ region far below the doubly magic ^{208}Pb has become accessible experimentally and represents a step further towards the study of heavy neutron-rich nuclei approaching the *r*-process waiting point at $A = 195$.

DOI: 10.1103/PhysRevC.89.024616 PACS number(s): 26.30.Hj, 25.70.Mn, 27.80.+w

I. INTRODUCTION

Radioactive nuclei play an important role in many cosmic phenomena, and information on these nuclei is particularly important to improve our understanding of the processes that shape our universe. In particular, one of the major challenges of nuclear astrophysics is to explain how the heavy elements are created in the universe. The rapid neutron-capture process (*r*-process) [1,2] of nucleosynthesis is thought to be responsible for the production of half of the amount of matter in the universe in the Z range above iron. Starting with a seed nucleus, neutron-rich nuclides are produced via a series of neutron captures until a point is reached where an equilibrium is established between the neutron-capture and the photodisintegration reactions. Here, the *r*-process essentially stalls until this *waiting-point* nucleus undergoes a β decay, and the capture of neutrons can then continue until another equilibrium is established. Once neutron capture ceases, the unstable nuclides β decay towards the valley of stability, forming the *r*-process nuclei. As early as 1957, Burbidge *et al.* [1] pointed out that the *r*-process passes through neutron-magic nuclei around $A = 80$, 130, and 195 which have longer-than-average β-decay half-lives. Besides this basic understanding, the astrophysical scenarios in which an *r*-process may occur are still a matter of debate, due to the high density of free neutrons required per seed nucleus to run this process through far-unstable nuclei, such as $^{80}Zn_{50}$, $^{130}Cd_{82}$, and $^{195}Tm_{126}$, up to the heaviest elements in nature. Experimental studies of very neutron-rich nuclides lying on and near the *r*-process path provide direct data for use in *r*-process nucleosynthesis calculations and to test current theories from which nuclear properties of far-unstable isotopes are derived.

The production of heavy neutron-rich nuclei in the laboratory has been a challenging problem in the last decades. Very neutron-rich nuclei are unstable, and the more exotic they are, the shorter their half-lives. The battle which faces the physicist is thus the need for high enough yields of such unstable nuclei, despite their generally low-production cross sections and extremely short half-lives. Neutron-rich nuclei can be produced by several physical processes such as quasielastic and deep inelastic transfer of some nucleons, fragmentation, and fission. However, deep inelastic or multinucleon transfer can only be applied with thin targets, limiting the final production rates. Fragmentation and fission seem to be better-suited reaction mechanisms that allow a large variety of neutron-rich nuclei to be produced.

Since the discovery of fission in 1938, a large variety of neutron-rich nuclei has been produced by this reaction mechanism. As early as the late 1970s more than 400 new isotopes became accessible through fission [3]. However, the direct separation and investigation of heavy fission fragments by recoil-in-flight separation were impossible due to the broad ionic charge distribution of fission products and the limitation of the Z resolving power at low energies. During the late 1980s and 1990s, with the arrival of relativistic ion beams, important progress was made. The seminal works performed at the Gesellschaft für Schwerionenforschung (GSI), Darmstadt, Germany [4,5], allowed the identification of more than 100 new nuclear species by bombarding Pb and Be targets with a beam of ^{238}U with an energy of 750 A MeV. Recently, the in-flight fission of a 345 A MeV ^{238}U beam has been studied at the next-generation facility RIBF at the RIKEN Nishina

[*]Permanent address: Centre d'Etudes Nucléaires de Bordeaux Gradignan (CENBG), UMR 5797 IN2P3/CNRS-Université Bordeaux, F-33170 Gradignan, France; kurtukia@cenbg.in2p3.fr

[†]Present address: KIT-INE, Hermann-von-Helmholtz-Platz 1, D-76344 Eggenstein-Leopoldshafen, Germany.

[‡]Present address: Universidade de Vigo, E-36310 Vigo, Spain.

[§]Present address: Los Alamos National Laboratory, Los Alamos, New Mexico 87544, USA.

[‖]Present address: NSCL-MSU, 1 Cyclotron, East Lansing, Michigan 48824, USA.

[¶]Present address: INRNE, 72 Tzarigradsko chausee, BG-1784 Sofia, Bulgaria.

Center, Japan [6], where 45 new medium-mass neutron-rich nuclei were observed.

Fragmentation reactions have also proven to be a well-suited reaction mechanism for producing heavy neutron-rich nuclei. While fission produces higher yields for medium-mass neutron-rich nuclei, fragmentation is the optimal solution for light and heavy neutron-rich nuclei. One recent example of fragmentation reactions is the discovery of neutron-rich nuclei using a relativistic ^{238}U beam at 1 A GeV impinging on a Be target [7,8] at GSI. Altogether 90 heavy neutron-rich nuclei were identified for the first time in these works in the atomic number range of $60 \leqslant Z \leqslant 87$. This region of the chart of nuclides is particularly important for understanding the astrophysical *r*-process of nucleosynthesis.

The present work focuses on the production of heavy neutron-rich nuclei by projectile fragmentation, in particular, in cold-fragmentation reactions [9]. These are projectile-fragmentation reactions at relativistic energies where mostly protons are abraded from the projectile, while the excitation energy induced is below the particle evaporation threshold. Therefore, these collisions lead to final residues with the same or almost the same neutron number as the projectile but a smaller atomic number. Cold fragmentation seems to be a well-suited reaction mechanism for producing very heavy neutron-rich nuclides, which cannot be obtained by fission. When using a ^{208}Pb beam, this reaction mechanism allows the production of heavy neutron-rich nuclei along the closed shell, $N = 126$, i.e., around the waiting point at $A = 195$. The identification of 26 new heavy neutron-rich nuclei below ^{208}Pb has been reported by us before [10–13]. In this paper we report the production cross sections of these nuclides together with another 169 cross sections of heavy neutron-rich nuclei produced by the in-flight fragmentation of relativistic ^{208}Pb projectiles.

II. EXPERIMENTAL PROCEDURE

The experimental data reported in the present work corresponds to an experiment performed at GSI. The experimental technique used for the production of heavy neutron-rich nuclei is in-flight fragmentation of relativistic heavy projectiles. The beam used was ^{208}Pb impinging on a beryllium target. The experiment requires the use of a heavy-ion accelerator to provide the relativistic primary beam and a high-resolution magnetic spectrometer to avoid any ambiguity when identifying the projectile residues produced in the reaction. The SchwerIonen Synchrotron (SIS) [14] coupled with the Fragment Separator (FRS) [15] facility at GSI is best suited for this kind of experiment.

^{208}Pb beams are extracted from the ion source, preaccelerated, and then injected into the Universal Linear Accelerator (UNILAC), which accelerates primary beams up to 12 A MeV. The ions are then injected into the SIS, where they are further accelerated. A thin carbon foil at the entrance of the SIS is used to increase the charge state of the ions of interest and to be able to reach the desired final energy. Our experiment was performed at 1 A GeV. The ionic charge of the beam at the exit of the SIS was $q = +67$. The SIS was operated in the slow extraction mode. The beam cycle was about 10 s long, and the beam was extracted with a spill length of about 2 s. The beam intensity was varied between 10^5 and 10^7 ions/s, according to our needs. After acceleration, the beam was guided to the FRS experimental area through the extraction beam line. Two different ^{9}Be targets were used for measuring the heavy and the lighter fragments, with thicknesses of 1023 ± 3 and 2526 ± 1 mg/cm^2 respectively, both of them backed with a 221 mg/cm^2 Nb stripping foil.

The GSI FRS is a two-stage magnetic spectrometer that allows the identification in-flight of the isotopic species produced, by determining both the atomic number Z and the mass-to-charge ratio A/Z of each fragment passing through the FRS by measuring their magnetic rigidities, time-of-flight, and energy loss. In order to separate different elements with enough resolution and to disentangle the different ionic charge states, the degrader energy-loss method [16,17] is used, which takes into account the difference in magnetic rigidity between the two sections of the FRS.

The FRS detection equipment used in the present experiment is shown in Fig. 1. It consists of two plastic scintillation detectors (Sc2, Sc4), at the intermediate dispersive image plane (F2) and the final focal plane (F4), and a velocity degrader, followed by a Nb stripping foil of 108 mg/cm^2 at F2, two multisampling ionization chambers (MUSIC1 and MUSIC2) at F4, with a Nb stripping foil of 260 mg/cm^2 in between, and two multiwire proportional counters located as shown in the figure.

The data acquisition system is VME based and consists of a single branch within the GSI Multi-Branch System framework [18]. In order to increase the data recording rate, the different tasks (readout, event building, taping, etc.) are divided between two processors: a data sender and a data receiver. The data sender is a RIO-3 processor which resides in the FRS VME crate. The RIO-3 handles the readout of

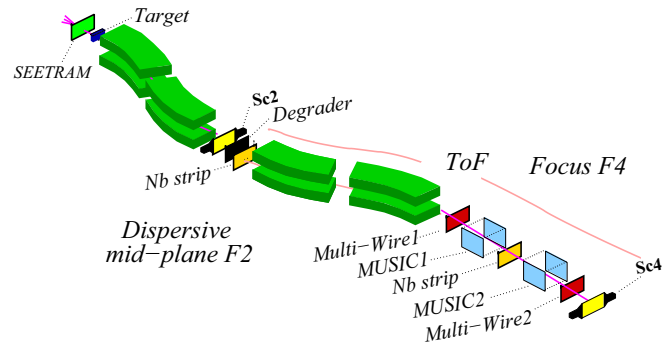

FIG. 1. (Color online) Schematic of the FRS experimental setup used in the present experiment. The beam monitor SEETRAM (Secondary Electron Transmission Monitor) and its calibration detector system (ionization chamber and scintillator Sc01, placed after the SEETRAM but not shown here) are located in front of the device. The target is located just in front of the first dipole. The FRS detector equipment consists of two plastic scintillation detectors (Sc2, Sc4), at the intermediate dispersive image plane (F2) and the final focal plane (F4), and a velocity degrader, followed by a Nb stripping foil at F2, two ionization chambers (MUSIC1 and MUSIC2) at F4, with a Nb stripping foil in between, and two multiwire proportional counters located as shown.

the digitizers (ADCs, QDCs, etc.) and then passes the data on via TCP/IP to a Lynx-OS PC, which acts as the data receiver. The latter formats the events, makes these available to analysis clients (e.g., via a remote event server), and controls taping or disk storage. Two triggers have been defined, aiming at reading the standard FRS equipment detectors for calibration (read-all standard FRS detector) and performing cross-section measurements [multiwire proportional counters and ionization chamber for Secondary Electron Transmission Monitor (SEETRAM) calibration not read]. In both cases the acquisition was triggered using scintillator Sc4 and a 10-Hz clock. These triggers were controlled via the acquisition trigger module in the FRS CAMAC crate.

A. Isotopic identification of projectile residues

The FRS, being a magnetic spectrometer, separates the fragments according to the ratio of mass number to ionic charge and the velocity, according to the magnetic rigidity

$$B\rho = \frac{A}{Q}\beta\gamma\frac{uc}{e}, \tag{1}$$

where B is the magnetic field (uniform and orthogonal to the particle trajectory), ρ is the deflection radius, A is the mass number, Q is the ionic charge number, e is the electron charge, c is the speed of light, u is the atomic mass unit, and $\beta\gamma$ is the reduced momentum from the relativistic parameters with $\beta = v/c$, where v is the velocity of the ion. Note that in this formula the precise mass of the ion is approximated by $A \cdot u$, neglecting the binding energy. For the purpose of isotopic identification, variations of the mass excess per nucleon with A/Z can be neglected and the aforementioned approximation for the mass of the ion can be assumed.

In order to determine the A/Z ratio, the magnetic rigidity $B\rho$, and the velocity v (through the time of flight in the second part of the FRS) of each ion must be measured. Since the velocity was measured in the second half of the spectrometer, the magnetic rigidity also had to be measured in the second section of the FRS. The former quantities can only provide the ratio of mass to ionic charge A/Q, according to Eq. (1), so we need to know not only the atomic number Z, but also the ionic charge state of the particle to define Q and to assign the correct mass.

The identification of heavy neutron-rich projectile fragments is a challenging task. Two issues must be overcome to obtain an unambiguous identification of fragments:

(i) contamination due to charge states produced inside the FRS and
(ii) loss of resolution in energy-loss measurements ΔE with the MUSIC chambers due to stochastic changes in charge states within the gas.

The use of a profiled aluminum degrader, placed at the intermediate focal plane of the FRS, and the combined measurement of the energy loss (ΔE) of the fragments in two MUSIC chambers, with a stripper foil in between, allowed us to separate all nonbare nuclei. A detailed description of this method can be found in Refs. [19] and [20]. Only a brief description is presented here.

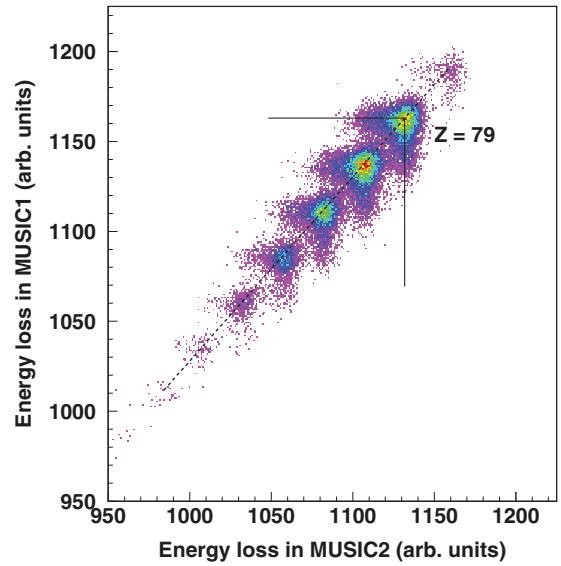

FIG. 2. (Color online) Scatterplot of the correlation between the energy-loss signals in the two ionization chambers for a setting of the FRS centered on ^{194}W.

The ionic charge state of heavy ions can change within the active region of the ionization chamber, and this effect contributes to the broadening of the energy-loss signal. The use of two ionization chambers allows us to make two independent measurements of the energy loss and to define an effective charge, with an improved resolution.

Figure 2 illustrates the correlation between the energy-loss signals of the two MUSICs. The probability of one ion's being fully stripped in at least one chamber was optimized with a Nb stripper foil placed in between. The observed double-wing pattern for each dot in Fig. 2 is due to the average ionic charge along the trajectory inside both ionization chambers. For each charge, the energy-loss signal in the horizontal wing corresponds to those ions which carry no electrons in the first chamber (MUSIC1). The vertical wing corresponds to the fully-stripped ions in the second chamber (MUSIC2). The wings overlap in cases of fully stripped ions in both chambers. The diagonal line passing through the different cores corresponds to those events for which the same ionic charge was measured by the two chambers; that is, the average ionic charge along the trajectory inside both ionization chambers is the same.

For each ion we can define a new value $Q(\mathrm{max})_{\mathrm{eff}}$ once the observed main diagonal of the charges has been established. This $Q(\mathrm{max})_{\mathrm{eff}}$ is the maximum of the amplitudes of the signals of the two MUSICs. Only if the ion maintains at least one electron in the path through the two chambers can it be misidentified. However, we can get information on the ionic charge states of the fragments in the two sections of the FRS by measuring the energy loss in the degrader. With the aforementioned method one cannot determine the ionic charge states themselves but can detect a change in the ionic charge state from the first to the second section of the FRS. If the

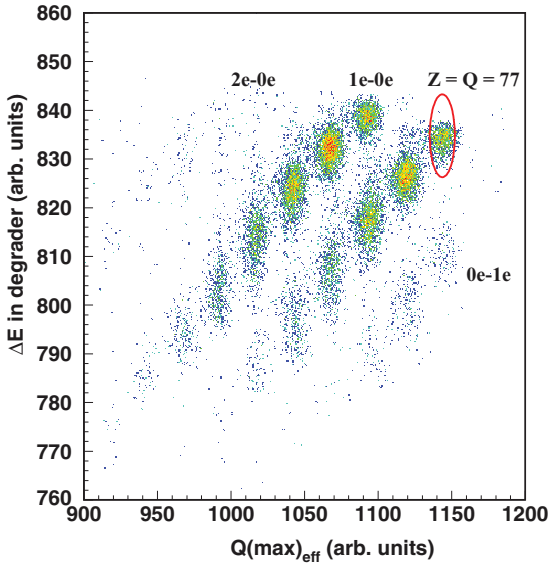

FIG. 3. (Color online) Scatterplot of the energy loss in the intermediate degrader in relation to the energy loss measured with the two ionization chambers $Q(\text{max})_{\text{eff}}$ corresponding to an FRS setting optimized to transmit ^{186}Lu.

magnetic spectrometer is set to select fully stripped fragments with a given A/Z ratio, H-like fragments (that is, fragments with one electron) with atomic number Z and mass $A - A/Z$ will also be transmitted in the case of heavy nuclei, as well as He-like fragments with mass $A - 2A/Z$, etc. The degrader energy-loss method allows for the separation of the different charge states and for the assignment of the ionic charge number Q and the atomic number Z of the fragments passing through the FRS.

In Fig. 3 we plot the energy loss in the degrader, calculated as described in Refs. [19] and [20] versus the effective charge measured by the combined measurement of the two MUSICs, for a magnetic setting of the FRS optimized to transmit ^{186}Lu. In the figure we see dots along four tilted lines. Dots that lie on the central diagonal line are the most populated ones and correspond to nuclei which are fully stripped along the whole FRS. Also, small contributions of ions which carry one electron or even two electrons in the two magnetic sections of the FRS populate these dots. For a given Z value, the dots above and below the former ones correspond to nuclei with one electron before the degrader and fully stripped after it and vice versa, respectively. The two-electron cases are also shown in Fig. 3. The most unfavorable cases when using this analysis are those nuclides with one or two electrons that do not change charge state throughout the whole FRS. The procedure in these cases fails in the assignment of the nuclear charge and also in the determination of the mass number A, but one can calculate this contribution quantitatively. In the present experiment, these events represent only 2% as calculated using the code GLOBAL [21].

Once the fully stripped ions are selected ($Q = Z$ condition verified) using the method described above, the mass and the atomic number can be identified with no ambiguity. One practical way of identifying the fragments is to plot the atomic number Z versus the A/Z ratio, calculated using Eq. (1) as shown in Fig. 4(a). This figure shows a two-dimensional cluster plot of the isotopes measured at two FRS settings optimized to transmit ^{194}W and ^{186}Lu. In this cluster plot each nucleus is represented by a dot. The solid line in the cluster plot represents the limits of the chart of nuclides before this experiment. The projection on the A/Z ratio is shown in Fig. 4(c) for a specific element by a condition on the energy-loss signal.

Alternatively, the fragments can be identified by plotting A/Z against the position at the intermediate focal plane [see Fig. 4(b)], which allows us to separate the different isotopes by their masses. The high resolution achieved in this experiment can be seen in the clear separation of dots corresponding to different isotopes. In the present work we were able to identify for the first time 26 heavy neutron-rich nuclei. Table I summarizes the new isotopes.

III. PRODUCTION CROSS SECTIONS

The production cross sections are determined by three independent magnitudes: the total yields of individual fragments n_f, the total number of impinging projectiles n_p, and the number of atoms in the target n_t, as follows:

$$\sigma_{A,Z} = \frac{n_f}{n_p \cdot n_t}. \tag{2}$$

The procedure explained in the previous section allows us to identify unambiguously the nuclei produced in the reaction on an event-by-event basis. The experimental setup and the analytical procedure introduce limitations to the isotopic identification. Different corrections have to be applied to the measured yields in order to obtain the actual yields of each nucleus. In the following sections, the determination of all these corrections applied is explained in detail.

A. Determination of impinging projectiles n_p

In order to measure absolute production cross sections, it is necessary to determine the total number of impinging projectiles. The SEETRAM was developed at GSI [22] to survey heavy-ion beam intensities.

SEETRAM operation is based on the emission of secondary electrons from thin metal foils by the passage of ions. It consists of three aluminum foils, each 10 μm thick, placed in vacuum, parallel to each other and orthogonal to the beam direction. The outer foils are connected to a positive voltage (+80 V), and the inner foil is insulated from the rest of the detector and connected to the ground via a current integrator.

When the beam passes through the SEETRAM, electrons close to the surface leave the inner foil, thus generating a current in the central layer which is measured by a current digitizer. The current digitizer consists of several stages: First, the input current (i) is transformed into a voltage (v). The fast analog output of this signal can be used as a monitor for measuring the extraction profile. Second, the signal passes a filter with a time constant of 1 s for reducing noise, and finally, the signal is digitized. The resulting quantity is proportional to the number of incoming particles. By changing the resistance of the i/v converter in the current digitizer from 10^4 to 10^{10} Ω,

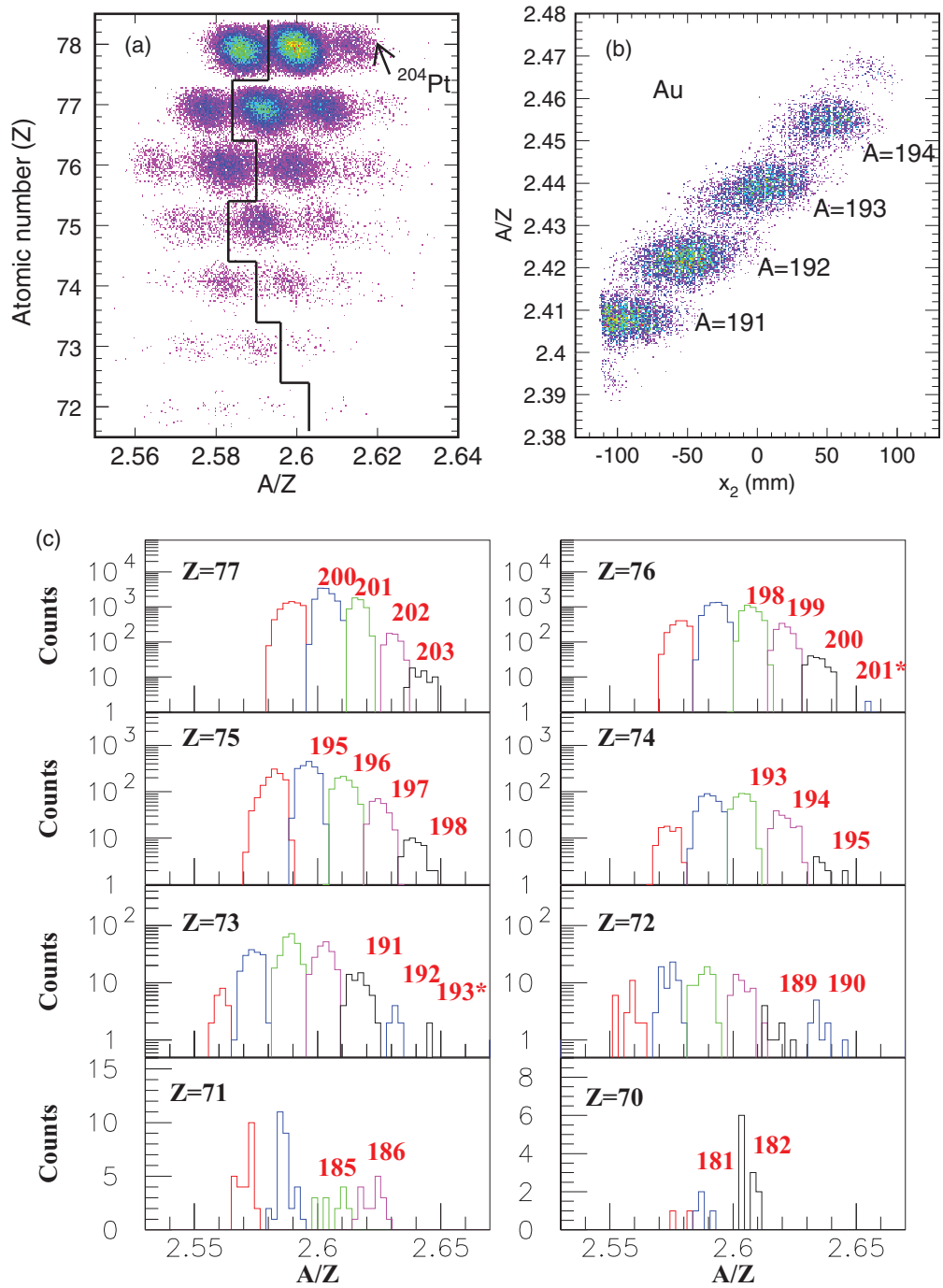

FIG. 4. (Color online) (a) Two-dimensional cluster plot of Z vs A/Z, containing the data corresponding to two different FRS settings, optimized to transmit ^{194}W and ^{186}Lu. The solid line represents the limits of the chart of nuclides before this experiment. (b) Two-dimensional cluster plot used for the identification of different gold isotopes, measured in one FRS setting optimized to transmit ^{188}Ir by plotting A/Z against the position at the intermediate focal plane. (c) Projection on the A/Z ratio from Ir to Yb corresponding to the data shown in (a). The newly identified isotopes are shown in red. For ^{201}Os and ^{193}Ta, indicated by asterisks, the transmission could not be properly determined (see Sec. III C 4), and only the limit to the absolute value of the cross section of these nuclei has been determined.

the sensitivity of the SEETRAM can be changed from 10^{-4} to 10^{-10} A per output pulse, allowing seven levels of sensitivity.

The current digitizer produces an adjustable constant offset current which allows us to identify any unwanted noise signal produced. Such background signals have to be subtracted from the number of counts in a spill in order to obtain the actual number of SEETRAM counts produced by the passage of the beam particles (see Fig. 5).

The SEETRAM yield not only depends on the ion species and the beam energy but also is sensitive to surface impurities. Long irradiation leads to a reduction in the secondary-electron yield in the region around the beam position. There-

TABLE I. New isotopes identified for the first time in this experiment.

Z	N	A	Z	N	A
78	126	204	75	120	195
78	125	203	74	121	195
77	126	203	74	120	194
77	125	202	74	119	193
77	124	201	73	120	193
77	123	200	73	119	192
76	125	201	73	118	191
76	124	200	72	118	190
76	123	199	72	117	189
76	122	198	71	115	186
75	123	198	71	114	185
75	122	197	70	112	182
75	121	196	70	111	181

fore, SEETRAM calibration has to be performed for every experiment.

The total thickness of the SEETRAM is 8.9 mg/cm^2 Al, and the nuclear-reaction probability is less than 0.1% for a ^{208}Pb beam at 1 A GeV. This makes it a very efficient beam monitor that has almost no influence on the beam quality and does not disturb the cross-section measurements.

The total number of impinging particles is given by

$$n_p = N_{\mathrm{SEETRAM}} \cdot f \cdot 10^{10} \cdot \mathrm{sensitivity} \tag{3}$$

where N_{SEETRAM} is the total number of SEETRAM counts with the background offset already subtracted, f is the calibration factor, and the *sensitivity* ranges from 10^{-4} to 10^{-10} A per output pulse as explained before.

Figure 6 shows the number of ^{208}Pb ions measured in scintillator Sc01 versus the number of SEETRAM counts. Sc01 is a scintillator placed in the beam-line setup after the SEETRAM only for calibration purposes. In contrast to the SEETRAM counts, the scintillator counts suffer from pileup of subsequent signals. To first order the number of counts in the scintillator depends quadratically on the beam intensity [22]. The first-order coefficient of the quadratic fit to the data represents the calibration factor.

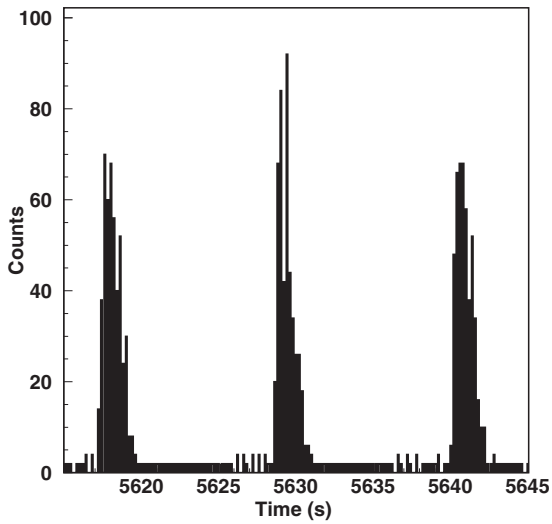

FIG. 5. SEETRAM counts over time, in a given time interval during the experiment. The constant offset current produced by the digitizer allows us to identify any unwanted noise signals.

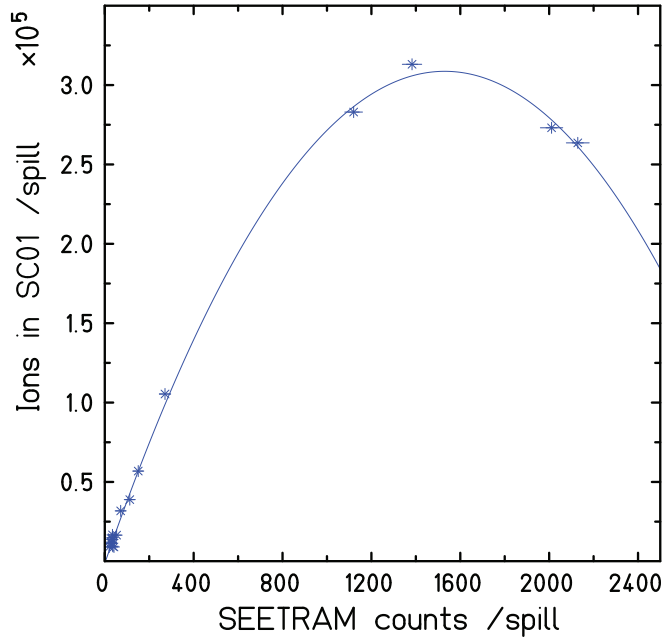

FIG. 6. (Color online) Number of ^{208}Pb ions measured in Sc01 versus the SEETRAM counts. Each point represents the result obtained for one spill. A quadratic fit is shown (see text for details).

In order to correctly determine the calibration factor, it is important to set correctly the upper limit of the number of SEETRAM counts included in the fit. If this upper limit is too low, the uncertainty of the linear calibration constant is quite high, while if this upper limit is too high, the assumption of a quadratic dependence is not true anymore, since the quadratic fit describes the observed trend only in the first-order approximation. In the latter case, the constant of the linear term deviates in a systematic way from the correct calibration factor.

The best way to determine this upper limit is to repeat the quadratic fit assuming different values of the upper limit of the SEETRAM counts. The value of the calibration factor is determined where the linear term coefficient is rather independent of the value of the upper limit set in the fit. The SEETRAM calibration factor obtained in the experiment was $f = 364 \pm 36$ ions/SEETRAM count. (See Ref. [11] for details.)

B. Determination of target atoms n_t

The number of target atoms per unit area n_t is given by

$$n_t = \frac{N_0 \cdot t}{A_t}, \tag{4}$$

where N_0 is Avogadro's number, t is the target thickness (in mg/cm^2), and A_t is the mass number of the target. The nature and thickness of the production target were chosen as

TABLE II. Probabilities of nuclear reactions and ionic charge states for targets used in the experiment as predicted by AMADEUS [23].

Thickness (mg/cm^2)	Nuclear reaction (%)	0e	1e	2e
1023	19.6	0.915	0.083	0.002
2526	41.6	0.894	0.103	0.003

a compromise between a maximized production of fragments and a low secondary-reaction rate.

We used two different ^{9}Be targets, with thicknesses of 1023 ± 3 mg/cm^2 for measuring heavy fragments and 2526 ± 1 mg/cm^2 for lighter ones, both of them having a 221 mg/cm^2 Nb stripper backing. The thickness of the targets represents ≈10%–20% of the range of the projectile, which provides the highest rate of projectile fragments [17], while the secondary-reaction probability is still supportable. The effect of the stripper backing the target is that the ionic charge distribution of the residues at the FRS entrance results in a large fraction of bare nuclei and small contributions of hydrogen-like or helium-like nuclei.

The expected number of nuclear reactions in these targets and the resulting charge-state distributions (as predicted with the code AMADEUS [23]) are summarized in Table II. The uncertainty of the probability of nuclear reactions is approximately 10% [24], and that for the charge-state distributions is 5% [25].

C. Yield determination n_f

The actual number of fragments produced is determined via the formula

$$n_f = Y_{\text{measured}} \cdot C_{\text{DAQ}} \cdot C_1 \cdot C_2 \cdot C_3 \cdot C_T, \qquad (5)$$

where C_{DAQ} is the correction factor due to the acquisition dead time; C_1 and C_2 are the correction factors due to losses of projectile nuclei in the target and for the fragments in the different layers of matter present in the beam-line setup, respectively; and C_3 is the correction factor due to ionic charge-state distributions in the experimental setup. If the transmission T through the FRS is not 100%, the transmission correction factor $C_T = 1/T$ also must be included in the calculation of the actual yields.

1. Dead-time correction: C_{DAQ}

For each event readout we register the number of triggers, that is, all signals, and the number of accepted triggers, that is, the number of fully processed ones. The ratio between these two magnitudes serves as a measure of the overall dead time of the detection system, so that

$$C_{\text{DAQ}} = \frac{N_{\text{free triggers}}}{N_{\text{accepted triggers}}}. \qquad (6)$$

During the experiment typical values of the dead-time range from 5% for the most exotic isotopic region to 30% for the regions close to the projectile, where the production rates are relatively high and the dead-time values are controlled by adjusting the beam intensity. The error of this correction is given by the square root of the quadratic sum of the roots of the registered "free" and "accepted" triggers. The uncertainty introduced by this correction ranges between 0.5% and 9%.

2. Corrections due to secondary reactions: C_1 and C_2

Losses for the projectiles in the target (C_1) as well as for the fragments in the different layers of matter (C_2) present in the beam-line setup were determined by calculating the total nuclear-reaction cross sections according to the microscopic model of Karol described in Ref. [26], so that $C_1 = 1/(1 - P_1)$ and $C_2 = 1/(1 - P_2)$, P_1 being the reaction probability of the projectile nuclei in half of the target thickness and P_2 the reaction probability of the fragments in half of the target thickness and in any other layer of matter downstream from the target. The main contribution to this correction factor is due to the plastic scintillator Sc2 and the degrader, situated at F2, which amounts to about 50%. The corresponding correction factor ranges between ≈2 and 2.1.

The error of the corrections of secondary reactions is directly dependent on the error of the total-reaction cross-section formula, which corresponds to 10%. The correction for the fragment residues includes only losses of fragments due to secondary reactions, since the magnetic rigidities of the products of secondary reactions at the intermediate focal plane are, in general, outside the acceptance of the second stage of the FRS, so these products will not be transmitted to the final focal plane and thus will not be detected.

3. Corrections due to ionic charge states: C_3

As explained before, the measured yields correspond to nuclei that are fully stripped along the FRS. All charge-state combinations different from 0e-0e must be included to determine the actual yields. This can be done by determining

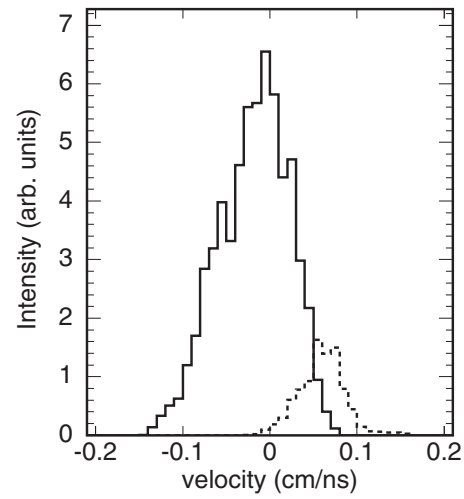

FIG. 7. Velocity distribution in the middle of the target, in the frame of the projectile, for the nucleus ^{206}Pb. The different areas correspond to the velocities measured with two different FRS magnetic settings. Overlapping these measurements allows us to reconstruct the whole velocity distribution.

TABLE III. Production cross sections (in mb) measured in the reaction ^{208}Pb(1 A GeV) + Be. Absolute errors include statistical and systematic uncertainties.

Z	A	σ	$\Delta\sigma$	Z	A	σ	$\Delta\sigma$	Z	A	σ	$\Delta\sigma$	Z	A	σ	$\Delta\sigma$
83	208	2.3×10^{-1}	6.1×10^{-2}	78	190	3.5	7.5×10^{-1}	75	183	6.0×10^{-1}	1.1×10^{-1}	71	186	2.9×10^{-6}	7.0×10^{-7}
83	207	1.4	3.0×10^{-1}	78	189	3.4	6.2×10^{-1}	75	182	8.5×10^{-1}	1.6×10^{-1}	71	185	6.9×10^{-6}	1.7×10^{-6}
83	206	2.5	6.2×10^{-1}	78	188	4.1	8.5×10^{-1}	74	195	3.2×10^{-6}	1.1×10^{-6}	71	184	1.9×10^{-5}	4.4×10^{-6}
83	205	5.2	1.4	77	203	3.9×10^{-6}	1.0×10^{-6}	75	184	4.1×10^{-1}	8.0×10^{-2}	72	175	1.6×10^{-1}	2.9×10^{-2}
82	207[a]	1.2×10^{2}	2.5×10^{1}	77	202	5.9×10^{-5}	1.2×10^{-5}	74	194	1.5×10^{-5}	3.6×10^{-6}	72	174	3.0×10^{-1}	5.4×10^{-2}
82	206[a]	5.4×10^{1}	1.1×10^{1}	77	201	5.6×10^{-4}	1.2×10^{-4}	74	193	4.2×10^{-5}	9.0×10^{-6}	71	183	4.1×10^{-5}	1.1×10^{-5}
82	205	4.0×10^{1}	7.2	77	200	1.7×10^{-3}	3.5×10^{-4}	74	192	1.0×10^{-4}	1.9×10^{-5}	71	182	1.1×10^{-4}	2.8×10^{-5}
82	204	3.0×10^{1}	5.4	77	199	2.9×10^{-3}	5.3×10^{-4}	74	191	2.1×10^{-4}	4.5×10^{-5}	71	181	2.7×10^{-4}	1.2×10^{-4}
82	203	2.4×10^{1}	4.3	77	198	5.6×10^{-3}	3.0×10^{-3}	74	190	6.3×10^{-4}	1.5×10^{-4}	71	180	6.8×10^{-4}	1.7×10^{-4}
81	207	2.1×10^{1}	3.8	77	197	3.7×10^{-2}	7.1×10^{-3}	74	189	2.1×10^{-3}	5.0×10^{-4}	71	179	1.5×10^{-3}	4.1×10^{-4}
81	206	1.8×10^{1}	3.3	77	196	5.8×10^{-2}	1.3×10^{-2}	74	188	5.2×10^{-3}	1.0×10^{-3}	71	178	3.0×10^{-3}	6.7×10^{-4}
81	204	1.8×10^{1}	3.3	77	195	9.2×10^{-2}	2.3×10^{-2}	74	187	1.0×10^{-2}	2.1×10^{-3}	71	177	4.8×10^{-3}	1.0×10^{-3}
81	203	1.3×10^{1}	2.7	77	194	1.6×10^{-1}	3.1×10^{-2}	74	186	1.7×10^{-2}	3.6×10^{-3}	71	176	8.6×10^{-3}	1.8×10^{-3}
81	202	1.7×10^{1}	3.1	77	193	2.7×10^{-1}	5.8×10^{-2}	74	185	2.9×10^{-2}	6.1×10^{-3}	71	175	1.5×10^{-2}	3.2×10^{-3}
81	201	1.7×10^{1}	3.1	77	192	3.8×10^{-1}	7.0×10^{-2}	74	184	4.8×10^{-2}	9.2×10^{-3}	71	174	2.2×10^{-2}	4.6×10^{-3}
81	200	1.5×10^{1}	3.1	77	191	6.0×10^{-1}	1.3×10^{-1}	74	183	8.0×10^{-2}	1.7×10^{-2}	71	173	4.2×10^{-2}	8.7×10^{-3}
80	206	5.3×10^{-1}	9.6×10^{-2}	77	190	9.0×10^{-1}	1.9×10^{-1}	74	182	1.3×10^{-1}	2.7×10^{-2}	71	172	6.4×10^{-2}	1.3×10^{-2}
80	205	1.2	2.5×10^{-1}	77	189	1.1	2.0×10^{-1}	74	181	2.1×10^{-1}	4.6×10^{-2}	71	171	9.9×10^{-2}	2.1×10^{-2}
80	204	2.3	4.8×10^{-1}	77	188	1.6	2.9×10^{-1}	74	180	3.1×10^{-1}	9.2×10^{-2}	71	170	1.9×10^{-1}	3.9×10^{-2}
80	202	3.0	6.3×10^{-1}	77	187	2.1	3.8×10^{-1}	74	179	4.8×10^{-1}	9.1×10^{-2}	70	182	3.6×10^{-6}	7.6×10^{-7}
80	201	5.1	9.3×10^{-1}	77	186	2.7	5.6×10^{-1}	74	178	7.5×10^{-1}	1.4×10^{-1}	70	181	1.3×10^{-5}	2.7×10^{-6}
80	200	6.4	1.2	76	201[b]	$>2.6\times10^{-7}$		73	193[b]	$>4.3\times10^{-7}$		70	180	4.1×10^{-5}	8.5×10^{-6}
80	199	7.1	1.3	76	200	1.6×10^{-5}	3.5×10^{-6}	73	192	4.0×10^{-6}	9.4×10^{-7}	70	179	7.9×10^{-5}	1.6×10^{-5}
80	198	8.5	1.8	76	199	4.7×10^{-5}	9.8×10^{-6}	73	191	1.6×10^{-5}	3.2×10^{-6}	70	178	1.7×10^{-4}	6.0×10^{-5}
80	197	8.7	1.8	76	198	2.1×10^{-4}	4.5×10^{-5}	73	190	4.8×10^{-5}	9.4×10^{-6}	70	177	3.3×10^{-4}	1.2×10^{-4}
79	205	1.2×10^{-2}	2.2×10^{-3}	76	197	6.6×10^{-4}	1.4×10^{-4}	73	189	1.0×10^{-4}	2.2×10^{-5}	70	176	8.7×10^{-4}	2.3×10^{-4}
79	204	8.0×10^{-2}	1.4×10^{-2}	76	196	2.1×10^{-3}	4.0×10^{-4}	73	188	2.7×10^{-4}	5.7×10^{-5}	70	175	1.9×10^{-3}	4.3×10^{-4}
79	203	1.6×10^{-1}	2.9×10^{-2}	76	195	4.8×10^{-3}	1.1×10^{-3}	73	187	6.0×10^{-4}	1.2×10^{-4}	70	174	3.2×10^{-3}	7.1×10^{-4}
79	202	4.0×10^{-1}	8.4×10^{-2}	76	194	1.5×10^{-2}	3.0×10^{-3}	73	186	1.3×10^{-3}	3.0×10^{-4}	70	173	5.8×10^{-3}	1.3×10^{-3}
79	201	6.4×10^{-1}	1.4×10^{-1}	76	193	2.7×10^{-2}	5.8×10^{-3}	73	185	4.0×10^{-3}	8.4×10^{-4}	70	172	1.7×10^{-2}	3.6×10^{-3}
79	200	9.3×10^{-1}	2.2×10^{-1}	76	192	5.0×10^{-2}	1.1×10^{-2}	73	184	6.9×10^{-3}	1.3×10^{-3}	70	171	3.2×10^{-2}	6.7×10^{-3}
79	199	1.3	2.5×10^{-1}	76	191	1.2×10^{-1}	2.5×10^{-2}	73	183	1.5×10^{-2}	2.8×10^{-3}	70	170	5.5×10^{-2}	1.1×10^{-2}
79	198	1.9	3.5×10^{-1}	76	190	1.7×10^{-1}	3.2×10^{-2}	73	182	2.5×10^{-2}	4.7×10^{-3}				
79	197	2.7	6.2×10^{-1}	76	189	2.4×10^{-1}	4.7×10^{-2}	73	181	4.3×10^{-2}	9.2×10^{-3}				
79	196	3.8	7.2×10^{-1}	76	188	3.9×10^{-1}	7.3×10^{-2}	73	180	6.2×10^{-2}	1.1×10^{-2}				
79	195	4.7	9.7×10^{-1}	76	187	6.1×10^{-1}	1.2×10^{-1}	73	179	9.6×10^{-2}	1.7×10^{-2}				
79	194	5.0	9.1×10^{-1}	76	186	8.2×10^{-1}	1.5×10^{-1}	73	178	1.9×10^{-1}	3.4×10^{-2}				
79	193	5.6	1.1	76	185	1.0	1.8×10^{-1}	73	177	3.1×10^{-1}	5.7×10^{-2}				
79	192	6.9	1.3	76	184	1.5	3.0×10^{-1}	73	176	4.6×10^{-1}	9.7×10^{-2}				
79	191	6.7	1.4	76	183	1.8	3.7×10^{-1}	72	190	1.3×10^{-6}	3.7×10^{-7}				
78	204	2.7×10^{-4}	6.2×10^{-5}	75	198	5.0×10^{-6}	1.1×10^{-6}	72	189	3.8×10^{-6}	8.4×10^{-7}				
78	203	2.5×10^{-3}	5.2×10^{-4}	75	197	2.8×10^{-5}	5.3×10^{-6}	72	188	9.9×10^{-6}	2.1×10^{-6}				
78	202	1.1×10^{-2}	2.3×10^{-3}	75	196	9.0×10^{-5}	1.7×10^{-5}	72	187	3.1×10^{-5}	6.8×10^{-6}				
78	201	2.7×10^{-2}	5.6×10^{-3}	75	195	2.4×10^{-4}	4.5×10^{-5}	72	186	7.3×10^{-5}	2.0×10^{-5}				
78	200	8.9×10^{-2}	1.7×10^{-2}	75	194	4.5×10^{-4}	9.4×10^{-5}	72	185	2.2×10^{-4}	8.0×10^{-5}				
78	199	1.4×10^{-1}	2.6×10^{-2}	75	193	1.3×10^{-3}	2.5×10^{-4}	72	184	4.5×10^{-4}	1.3×10^{-4}				
78	198	2.6×10^{-1}	6.2×10^{-2}	75	192	3.8×10^{-3}	7.3×10^{-4}	72	183	7.8×10^{-4}	1.9×10^{-4}				
78	197	4.9×10^{-1}	1.2×10^{-1}	75	191	7.6×10^{-3}	1.8×10^{-3}	72	182	2.2×10^{-3}	5.4×10^{-4}				
78	196	7.6×10^{-1}	1.6×10^{-1}	75	190	1.8×10^{-2}	4.4×10^{-3}	72	181	5.0×10^{-3}	9.8×10^{-4}				
78	195	9.2×10^{-1}	1.7×10^{-1}	75	189	3.3×10^{-2}	8.7×10^{-3}	72	180	9.2×10^{-3}	1.7×10^{-3}				
78	194	1.4	2.9×10^{-1}	75	188	4.7×10^{-2}	1.0×10^{-2}	72	179	2.1×10^{-2}	3.9×10^{-3}				
78	193	1.8	3.7×10^{-1}	75	187	8.4×10^{-2}	1.9×10^{-2}	72	178	3.4×10^{-2}	6.3×10^{-3}				
78	192	2.4	5.0×10^{-1}	75	186	1.6×10^{-1}	4.1×10^{-2}	72	177	5.7×10^{-2}	1.4×10^{-2}				

[a]The total measured cross section on Be/Nb is 140 ± 25 for ^{207}Pb and 62 ± 11 mb for ^{206}Pb. See Sec. III C 5 for details.

[b]The transmission correction could not be evaluated. Only a limit on the cross section is given.

the survival probability for the fully stripped fragments $P_{0\text{-}0}$, and thus the correction factor C_3 is given by $C_3 = 1/P_{0\text{-}0}$. The GLOBAL [21] calculation contains a refined parametrization of charge-exchange cross sections depending on the target, projectile, energy, and electronic shells. A calculation was done for the reaction ^{208}Pb(1 A GeV) + Be including all the detectors present in the experimental setup, and the yields of each fragment were corrected accordingly. The uncertainty introduced by this correction amounts to 5%. Typical values for this correction range from 1.4 for the lightest fragments ($Z = 71$) to 2.5 for heavier ones ($Z = 83$).

4. Transmission through the FRS: C_T

The FRS is limited to ±1.5% in momentum acceptance and to 15 mrad in angle. The transmission of a given nucleus at a certain energy is defined by these two factors and the position of the fragment distribution at the intermediate and final focal planes.

The typical angular distribution of the measured fragmentation residues in this experiment is below 5 mrad [27]. This means that the transmission is close to 100%. This effect will only be important for nuclei that are transmitted to the edges of the focal plane positions. This limitation is overcome in most cases by the overlap of different magnetic settings of the FRS and the reconstruction of the longitudinal velocity distributions, by comparing, channel by channel, all velocity distributions measured for a given nucleus and taking the maximum value. Since the reaction cross section does not vary in accordance with the small variation in energy that the beam experiences (due to the finite thickness of the target material), the position where the fragment is formed is thus, on average, the middle of the target. The fragment velocity is then calculated in the middle of the target with the help of AMADEUS in the reference frame of the beam, using the Lorentz transformations.

Figure 7 shows the velocity distribution in the projectile frame for the nucleus ^{206}Pb. The different areas correspond to the normalized data recorded with two different FRS magnetic settings, each contributing to the reconstruction of the whole velocity distribution.

Only for cases in which the overlap is not enough to reconstruct the full velocity distributions are the fragment position distributions at the intermediate and final focal planes fitted to a Gaussian to obtain the transmission T, and the transmission correction factor $C_T = 1/T$ included in the normalization of the yields. This procedure gives an overall uncertainty of 20% for the transmission correction factor. When this correction could not be determined (edge transmission and low counting rate), the cross sections reported in this paper should be assumed to represent the lower limit to the absolute value.

5. Electromagnetic dissociation (EMD) correction

The relative motion of a projectile nucleus traveling at relativistic energies with respect to the target nucleus can give rise to an increasingly hard spectrum of virtual photons. These virtual photons can excite the dipole and quadrupole giant resonances of the projectile. The excitation energy associated with this energy exchange can result in the liberation of nucleons, mainly by the emission of one or two neutrons. This process, EMD, is discused in detail in Ref. [28].

In general, the EMD is negligible in comparison to the nuclear-reaction probability, but for heavy targets it should be taken into account. In our experiment the beryllium target has a niobium backing foil of 221 mg/cm^2. The EMD cross section on the beryllium target amounts to 18 mb, and that on the niobium stripping foil to 1272 mb, as calculated using ABRABLA [29], a Monte Carlo simulation code of the nuclear-reaction model. These contributions are not negligible and should be taken into account in the determination of the $1n$ and $2n$ loss cross sections. The EMD cross section of ^{207}Pb ($1n$ loss) on the niobium stripping foil amounts to 29% of the total cross section, and in the case of ^{206}Pb ($2n$ loss) it reaches 16%. These contributions are removed from the observed cross section of these nuclei. The values reported in Table III only include the EMD contribution of the beryllium target. The error associated with this calculation is considered to be 5% [30].

D. Results

All the fragment products measured in the present work are represented in the chart of nuclides in Fig. 8. They cover the region of heavy neutron-rich nuclei around the neutron closed shell $N = 126$, with elements ranging from Yb to Bi. The solid line in the figure indicates the limits of the chart of nuclides before this experiment. In the present work we were able to synthesize and measure the production cross -sections of more than 190 heavy neutron-rich residues, 26 of which were observed for the first time.

Table III lists the data on the measured cross sections together with the absolute errors (including both statistical and systematical uncertainties). The statistic uncertainty is determined by the width of the Poisson distribution of the

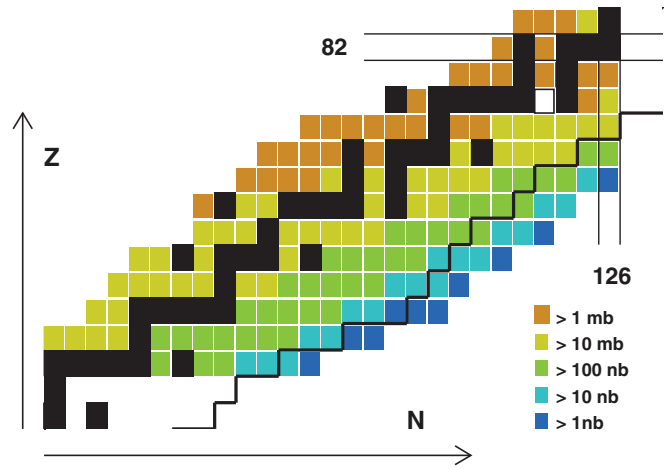

FIG. 8. (Color online) Measured production cross sections of the fragment residues in the reaction ^{208}Pb(1 A GeV) + Be. The solid line represents the limits of the chart of nuclides before this experiment.

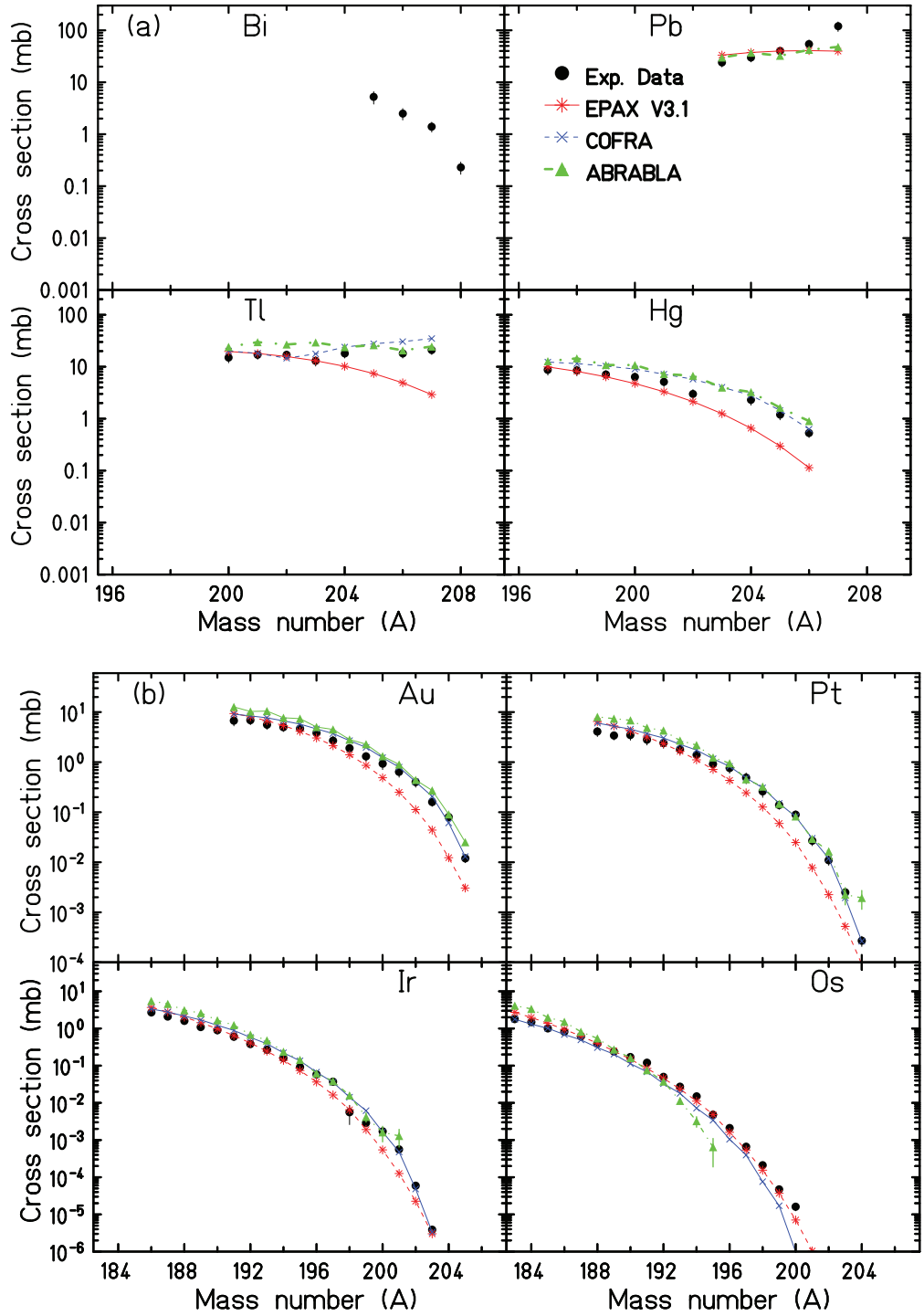

FIG. 9. (Color online) Measured isotopic production cross sections of fragment residues produced in the reaction ^{208}Pb(1 A GeV) + Be (filled black circles) compared with the EPAX parametrization [dashed (red) line with asterisks], the COFRA calculation [dotted (blue) line with X's], and ABRABLA [dashed-dotted (green) line with triangles]. (a) Close-to-the-projectile fragments from $Z = 83$ to $Z = 80$. (b) Fragments from $Z = 79$ to $Z = 76$. If not shown, the error bars of the experimental data and the ABRABLA calculation are smaller than the symbols.

accumulated statistics. The uncertainty associated with the different corrections applied for the correct determination of the cross sections, that is, the calibration of the SEETRAM counts, transmission correction, and correction for secondary reactions and charge states, has been pointed out in the discussion of each one of them. The relative uncertainty of the cross section is the quadratic sum of the uncertainties of the different components, statistical errors and systematic errors. The total relative uncertainty of the measured cross sections ranges between 17% and 26%.

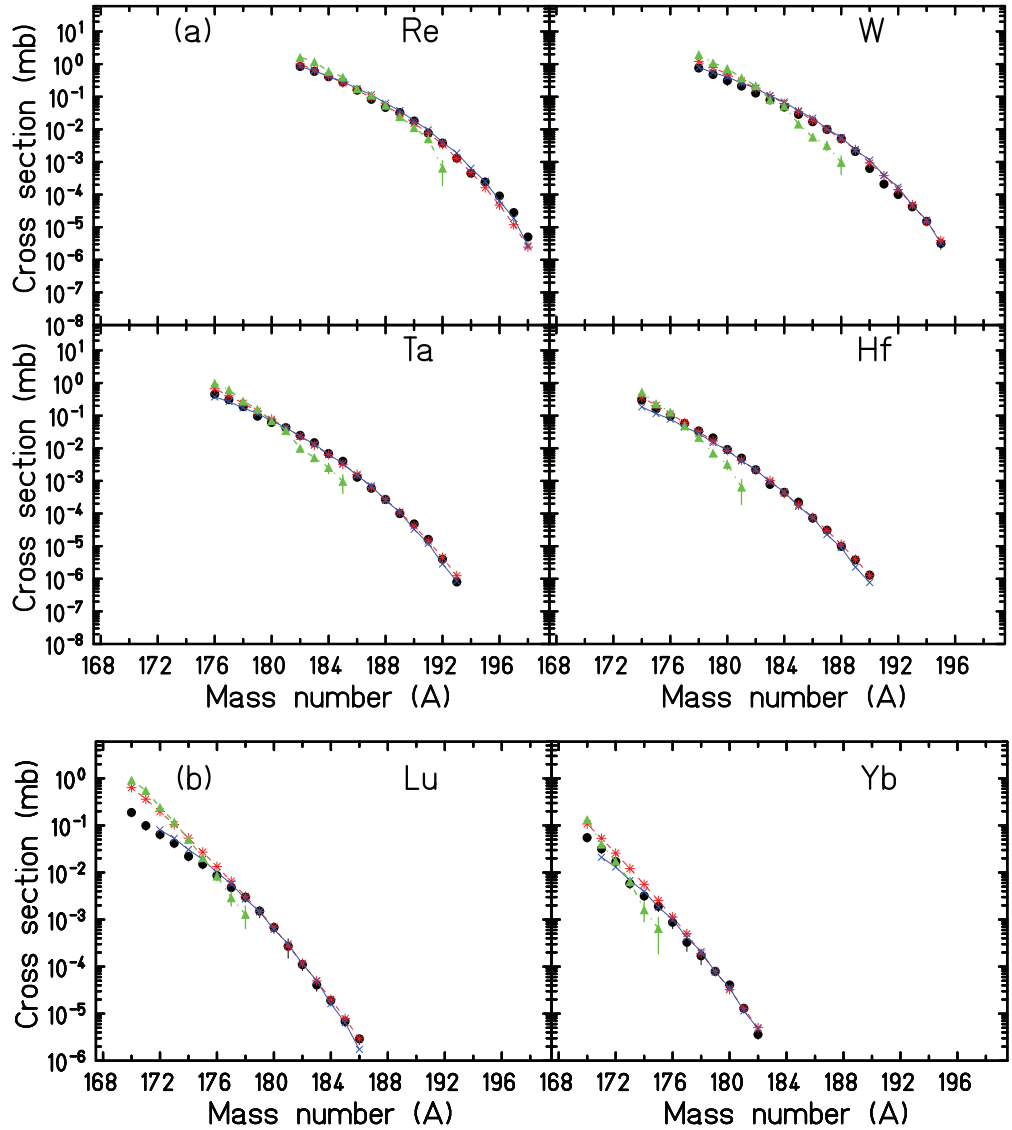

FIG. 10. (Color online) Measured isotopic production cross sections of fragment residues produced in the reaction ^{208}Pb(1 A GeV) + Be (filled black circles) compared with the EPAX parametrization [dashed (red) line with asterisks], the COFRA calculation [dotted (blue) line with X's], and ABRABLA [dashed-dotted (green) line with triangles]. (a) Fragments from $Z = 75$ to $Z = 72$. (b) Lighter fragments, $Z = 71$ and $Z = 70$. If not shown, the error bars of the experimental data and the ABRABLA calculation are smaller than the symbols.

IV. DISCUSSION OF EXPERIMENTAL RESULTS

A. Benchmark of nuclear fragmentation cross-section models

In order to estimate the number of fragments produced, computer codes of model descriptions of the fragmentation process have been developed. Among them we can highlight EPAX v.3 [31], a semiempirical parametrization of the fragmentation cross section; ABRABLA [29], a Monte Carlo simulation code of the nuclear-reaction model describing the nuclear-collision process for energies well above the Fermi energy; and the COFRA [9] code, an analytical version of ABRABLA.

In order to give an overview of the predictive power of the different calculations in the region of the heavy neutron-rich nuclei, in Figs. 9 and 10 the calculated isotopic distributions of EPAX, ABRABLA, and COFRA are compared with the measured data.

EPAX is an empirical parametrization of the fragmentation cross sections based on experimental data on fragmentation reactions of medium- to heavy-mass projectiles. Since cross sections of very neutron-rich fragments became available (e.g., in the present experiment), the well-known EPAX parametrization has been further developed and is now able to give very realistic predictions also in these cases. As EPAX is not aimed for pickup reactions, in Fig. 9 no predictions are shown for Bi isotopes. For Pb isotopes, a good agreement is observed except for the $1n$ loss channel. The isotopic distributions of the close-to-projectile fragments from Tl to Ir are very well reproduced except for masses approximately $\geqslant$200. This region is influenced by the proton-to-neutron ratio

of the projectile, which is lost for the fragments located in the evaporation-residue corridor. The isotopic distributions far away from the projectile, from Os to Yb, show a remarkably good agreement with the experimental data for both neutron-rich and neutron-deficient fragments.

The abrasion-ablation Monte Carlo code ABRABLA shows a fair overall agreement with the data, not only for the most neutron-rich nuclei but also for the neutron-deficient ones, both near and far from the projectile. As in the case of EPAX, no pickup reactions are included, and thus no comparison can be done for Bi isotopes. Again, for the $1n$ loss, a disagreement is observed. Below 0.5 μb no predictions could be obtained due to prohibitive computing times. The number of simulated events was 10^7, which took 5 days of computing time.

The disagreement observed between the experimental cross sections for the $1n$ loss channel may be attributed to EMD. In the EPAX calculation this effect is not included. In the case of the ABRABLA calculations shown here, it is taken into account by using the harmonic approximation [34]. However, in experiments using a ^{208}Pb projectile beam at 640 A MeV an enhancement of the measured cross section by a factor of 1.33(16) compared to the calculations in the harmonic approximation has been observed (see [35] and references therein). This enhancement is attributed to the excitation of the two-phonon isovector giant dipole resonance. This effect could explain part of the enhancement of the cross section of ^{207}Pb observed in the present work. Also, the charge-exchange reactions which are not included in these calculations could have some influence on the $1n$ loss cross section.

In cases where proton evaporation is negligible (which is the case for the very neutron-rich fragments considered here), the physics of ABRABLA can be formulated analytically. This makes it possible to calculate cross sections without any lower limit, avoiding the statistical uncertainties of the Monte Carlo code ABRABLA. COFRA is an analytical description based on the cold abrasion of protons and neutrons and on neutron evaporation. The predictions of this code are compared with the experimental data and a remarkably good description of the full data set is obtained. This calculation is very fast compared with Monte Carlo codes and is in good agreement with ABRABLA calculations. Note that ABRABLA and COFRA were not specifically adjusted to the very neutron-rich fragments as is the case for the EPAX code.

In summary, it seems that the fundamental processes in fragmentation reactions are rather well understood, since the predictions of the different fragmentation-reaction codes allow a good description of the production cross sections over a wide range of charges and masses, and therefore, it is possible to give a good estimate of the beam intensities for the different secondary-beam experiments.

B. Proton-removal channels

The use of fragmentation reactions allows for the production of a large variety of radioactive beams. The fragmentation reactions present large fluctuations in the N/Z value and excitation energies of the prefragments. These fluctuations

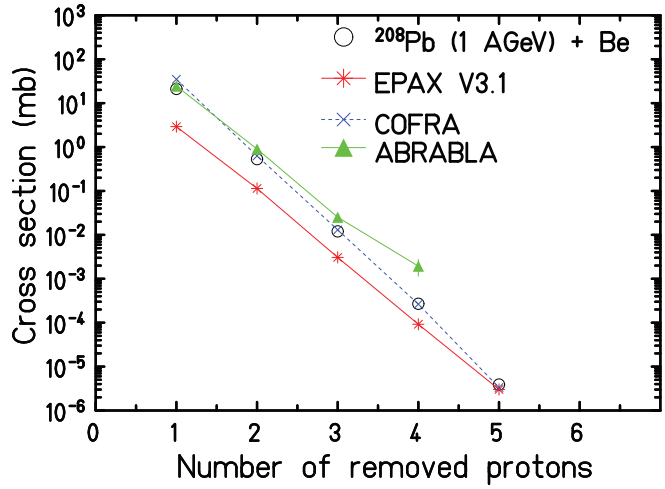

FIG. 11. (Color online) Production cross sections of the proton-removal channels measured in the reaction ^{208}Pb(1 A GeV) + Be (open black circles; this work), compared with the EPAX parametrization [solid (red) line with asterisks], the COFRA calculation [dotted (blue) line with X's], and ABRABLA [solid (green) line with triangles]. If not shown, the error bars of the experimental data and the ABRABLA calculation are smaller than the symbols.

can populate the *proton-removal channels*. In these reaction channels the projectile only loses protons in the fast nucleon-nucleon interaction, while the excitation energy is below the particle evaporation threshold. The limited energy that characterizes these channels earns this process the name cold fragmentation. These are the most neutron-rich nuclides one can observe using the experimental procedure described in this work, if one does not consider charge-exchange reactions, which have recently been proposed to produce nuclei with a larger neutron excess than those produced in fragmentation [36].

The measured proton-removal cross sections in the experiment are plotted in Fig. 11, including a comparison with EPAX predictions, ABRABLA, and COFRA. As can be seen, the three codes reproduce the tendency of the data fairly well. Nonetheless, one can observed that only COFRA and ABRABLA follow the data points closely, while EPAX is one order of magnitude off close to the projectile.

The experimental cross sections were also compared with different combinations of target/projectile using experimental data on previous measurements available in the literature. In Fig. 12(a), it can be observed that the data for ^{208}Pb do not show any characteristic change with respect to other targets used. The same effect is observed when comparing reactions induced by different heavy ions over the same target material [Fig. 12(b)]. Actually, all the results shown are compatible within the error bars. Therefore, we can conclude that in this energy regime the target does not influence appreciably the production of the proton-removal channels for a given projectile. It is important to take into account that in all investigated reactions the A/Z of the projectiles is rather similar. In reactions with projectiles with different A/Z values, this universal behavior could not be valid.

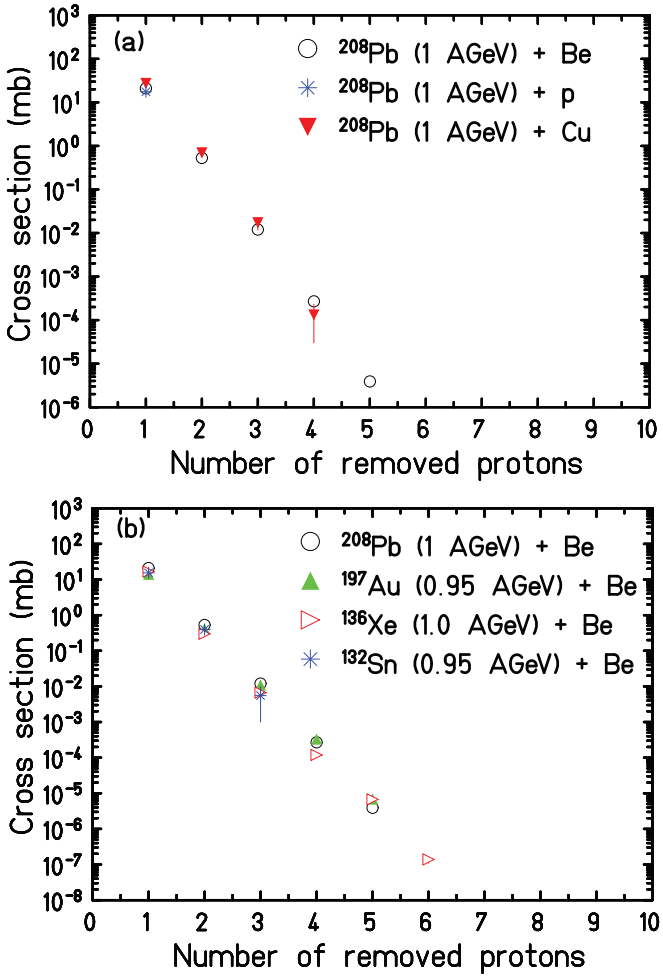

FIG. 12. (Color online) Production cross sections of the proton-removal channels measured in several heavy-ion reactions. (a) ^{208}Pb(1 A GeV) + Be (open circles; this work), ^{208}Pb(1 A GeV) + p (asterisks) [32], and ^{208}Pb(1 A GeV) + Cu (triangles) [33]. (b) ^{208}Pb(1 A GeV) + Be (open circles; this work), ^{197}Au(0.950 A GeV) + Be (filled upward triangles) [9], ^{136}Xe(1 A GeV) + Be (open rightward triangles) [37], and ^{132}Sn (0.950 A GeV) + Be (asterisks) [38]. If not shown, the error bars of the experimental data are smaller than the symbols.

V. CONCLUSIONS AND OUTLOOK

In the present work we have shown that fragmentation reactions using a ^{208}Pb beam at 1 A GeV impinging on a beryllium target allow for the production of neutron-rich nuclei along and near the neutron closed shell $N = 126$. The use of a high-resolution magnetic spectrometer FRS allowed us to identify more than 190 heavy neutron-rich nuclei produced in this reaction and to measure with a high accuracy the production cross sections up to a few nanobars. This work forms part of the seminal work performed at GSI for exploring the production of medium-mass and heavy neutron-rich isotopes by fragmentation [7,9,37].

With some exceptions close to the projectile, the predictions of the different fragmentation-reaction codes such as ABRABLA and COFRA as well as the EPAX code allow a good description of the production cross sections over a wide range of charges and masses, and therefore it is possible to give a good estimate of the beam intensities for the different secondary-beam experiments, which are essential in planning experiments on nuclei located at the outermost borders of the chart of nuclides.

The present findings represent a step further in investigations of heavy neutron-rich nuclei. The study of the properties of nuclei in this region holds a double interest: on the one hand, it is important for the understanding of the astrophysical r-process close to the waiting point $A = 195$ and to reproduce the abundance patterns; and on the other hand, we can study the robustness of the closed shell $N = 126$ far below the doubly magic ^{208}Pb and the evolution of collective structures and shapes. As the production rates will increase at facilities such as RIBF in Japan [39], FAIR in Germany [40], and FRIB [41] in the United States, more detailed information on these nuclei, such as their decay properties, shapes, and single-particle structure, could be studied.

ACKNOWLEDGMENTS

The authors are indebted to the GSI accelerator staff for providing an intense and stable beam of ^{208}Pb and to the GSI target laboratory and FRS colleagues for technical support. We also gratefully acknowledge Aleksandra Kelic for help with ABRABLA calculations. T.K.-N. acknowledges the support from Xunta de Galicia, Dirección Xeral de Investigación, Desenvolvemento e Innovación (Bolsa Predoutoral, Consellería de Innovación e Industria), and Universidade de Santiago de Compostela through Ph.D. studies. This work was partially supported by the European Community under FP6 Integrated Infrastructure Initiative EURONS Contract No. RII3-CT-2004-506065, the Spanish Ministry of Science and Innovation under Grant No. FPA2007-62652, the program Ingenio 2010, Consolider CPAN, and Xunta de Galicia under Grant No. PGIDT00PXI20606PM.

[1] E. M. Burbidge, G. R. Burbidge, W. A. Fowler, and F. Hoyle, Rev. Mod. Phys. **29**, 547 (1957).
[2] A. G. W. Cameron, CRL-41 (Atomic Energy of Canada, Ltd., Chalk River, Ont., Canada, 1957).
[3] T. von Egidy, *Nuclear Spectroscopy of Fission Products* (Institute of Physics, Bristol, UK, 1979), p. 51.
[4] M. Bernas *et al.*, Phys. Lett. B **331**, 19 (1994).
[5] M. Bernas *et al.*, Phys. Lett. B **415**, 111 (1997).
[6] T. Ohnishi *et al.*, J. Phys. Sci. Jpn. **79**, 073201 (2010).
[7] H. Alvarez-Pol *et al.*, Phys. Rev. C **82**, 041602(R) (2010).
[8] J. Kurcewicz *et al.*, Phys. Lett. B **717**, 371 (2012).
[9] J. Benlliure *et al.*, Nucl. Phys. A. **660**, 87 (1999). http://www.usc.es/genp/cofra.
[10] T. Kurtukian-Nieto *et al.*, in *International Symposium on Nuclear Astrophysics—Nuclei in the Cosmos—IX*, Proceedings of Science POS(NIC-IX)008 (2006).
[11] T. Kurtukian-Nieto, Ph.D. thesis, Universidade de Santiago de Compostela, 2006.

[12] T. Kurtukian-Nieto *et al.*, Nucl. Phys. A **827**, 587c (2009).
[13] T. Kurtukian-Nieto, J. Phys. Conf. Ser. **202**, 012012 (2010).
[14] M. Steiner *et al.*, Nucl. Instr. Meth. A **312**, 420 (1992).
[15] H. Geissel *et al.*, Nucl. Instr. Meth. B **70**, 286 (1992).
[16] J.-P. Dufour *et al.*, Nucl. Instr. Meth. A **248**, 267 (1986).
[17] K.-H. Schmidt *et al.*, Nucl. Instr. Meth. A **260**, 287 (1987).
[18] Multi-Branch System; http://www-w2k.gsi.de/daq/.
[19] J. Taïeb *et al.*, Nucl. Phys. A **724**, 413 (2003).
[20] E. Casarejos *et al.*, Phys. Rev. C **74**, 044612 (2006).
[21] C. Scheidenberger *et al.*, Nucl. Instr. Meth. B **142**, 441 (1998).
[22] C. Ziegler, Diploma thesis, Technische Hochschule Darmstadt, 1992; A. Junghans *et al.*, Nucl. Inst. Meth. A **370**, 312 (1996).
[23] AMADEUS; http://www-win.gsi.de/charms/amadeus.htm.
[24] C. J. Benesh, B. C. Cook, and J. P. Vary, Phys. Rev. C **40**, 1198 (1989).
[25] T. Brohm, Ph.D. thesis, Technische Hochschule Darmstadt, 1994.
[26] P. J. Karol, Phys. Rev. C **11**, 1203 (1975).
[27] J. Benlliure, J. Pereira-Conca, and K.-H. Schmidt, Nucl. Instr. Meth. A **478**, 493 (2002).
[28] T. Aumann *et al.*, Z. Phys. A **352**, 163 (1995).
[29] J.-J. Gaimard and K.-H. Schmidt, Nucl. Phys. A **531**, 709 (1991).
[30] J. Taieb, Ph.D. thesis, Université Paris Sud, 2000.
[31] K. Sümmerer, Phys. Rev. C **86**, 014601 (2012).
[32] T. Enqvist *et al.*, Nucl. Phys. A **686**, 481 (2001).
[33] M. de Jong *et al.*, Nucl. Phys. A **628**, 479 (1998).
[34] K.-H. Schmidt *et al.*, Nucl. Phys. A **665**, 221 (2000).
[35] K. Boretzky *et al.*, Phys. Lett. B **384**, 30 (1996).
[36] A. I. Morales *et al.*, Phys. Rev. C **84**, 011601 (2011).
[37] J. Benlliure *et al.*, Phys. Rev. C **78**, 054605 (2008).
[38] D. Perez-Loureiro *et al.*, Phys. Lett. B **703**, 552 (2011); D. Perez-Loureiro, Ph.D. thesis, Universidade de Santiago de Compostela, 2010.
[39] Y. Yano, Nucl. Instr. Meth. B **261**, 1009 (2007); http://www.nishina.riken.jp/RIBF.
[40] http://www.fair-center.de
[41] http://www.frib.msu.edu.